Supplementary Materials for

Significantly suppressing ion migration in metal halide perovskites via trace of multivalent interstitial doping

Yepin Zhao[1], Ilhan Yavuz[2*], Minhuan Wang [3], Marc H. Weber[4], Ju-Hong Lee[5], Shaun Tan[1], Tianyi Huang[1], Dong Meng[1], Rui Wang[1], Jingjing Xue[1], Sung-Joon Lee[6,7], Sang-Hoon Bae[8], Anni Zhang[1], Tae-Hee Han[1,9], Yifang Zhou[1], Jiming Bian[3], Nam-Gyu Park[5], Jin-Wook Lee[5*], Yang Yang[1*]

*Correspondence and requests for materials should be addressed to I.Y (email: ilhan.yavuz@marmara.edu.tr) or to J.-W. L. (email: jw.lee@skku.edu) or to Y.Y. (email: yangy@ucla.edu)

This PDF file includes:

Materials and Methods Supplementary Text S1-S2

Figures S1-S10

Tables S1-S7

Materials and solar cell fabrication

Neodymium trifluoromethanesulfonate ($(CF_3SO_3)_3Nd$, 98%), Calcium trifluoromethanesulfonate ($(CF_3SO_3)_2Ca$, 99.9%), Sodium trifluoromethanesulfonate ((CF_3SO_3) Na, 98%), dimethylsulfoxide (DMSO, 99.7%), isopropanol (IPA, 99.7%), dimethylformamide (DMF, 99.8%), acetone (99.9%), chlorobenzene (CB, 99.8%), acetonitrile (ACN, 99.8%), 4-tert-butyl pyridine (98%) and lithium bis(trifluoromethanesulfonyl)imide (Li-TFSI, 99.95%) were all purchased from Sigma Aldrich. Lead iodide beads (PbI2, 99.999%), SnO_2 colloidal solution (15% in water) were purchased from Alfa Aesar. Formamidine iodide (FAI), methylammonium iodide (MAI) were purchased from GreatCell Solar (Australia). Spiro-oMeTAD (99.8%) and methylammonium chloride (MACl) were purchased from Xi'an Polymer Light Technology in China. All the materials were used without further purification.

ITO glasses were firstly cleaned with detergent, deionized water, acetone and IPA for 30 minutes, respectively. Then, the ITO substrates were dried by the nitrogen gun and treated by UV-ozone for 20 minutes to remove organic residue on the surface. 0.2 mL of SnO_2 colloidal solution was diluted in 1.2 mL of deionized water and dropped on the pre-cleaned ITO glasses at a rate of 3000 rpm for 30 s, followed by annealing at 150 ℃ for 30 minutes in air. After cooled down to room temperature, the substrates were treated by the UV-ozone for another 10 minutes and transferred into the glovebox for the following steps. For the fabrication of perovskite films, a typical two-step method was employed here. 1.5 M of PbI_2 in DMF and DMSO (volume ratio is 9:1) was spin-coated onto the SnO_2 films at a rate of 1500 rpm for 30s and annealed at 90 ℃ for 5 min. For samples with passivation agents, additives with different molar ratio (0.02%, 0.05%, 0.08%, 0.10%, 0.15%, 0.20%, 0.25%, 0.30%,0.35%, 0.40%,0.45%, and 0.50%) to PbI_2 were added into 1 mL of PbI_2 precursors and the spin rate remained at 1500 rpm. The films were also annealed at 90 ℃ for 5 min. Organic salts of FAI: MAI: MACl (90 mg: 6.39 mg: 9 mg in 1 ml IPA) were spin-coated on PbI_2 films at a rate of 2000 rpm for 30s, followed with thermal annealing at 150 ℃ for 12 min in ambient air with a controlled humidity (30-40%). After cooled to room temperature, the perovskite films were transferred into glovebox for spiro deposition. 40 μL of spiro-oMeTAD solution, which consisted of 72.3 mg spiro-oMeTAD, 28.8 μl of 4-tert-butyl pyridine and 17.5 μL of lithium bis(trifluoromethanesulfonyl) imide (Li-TFSI) solution (520 mg Li-TSFI in 1 ml acetonitrile) in 1ml of chlorobenzene, was spin-coated on perovskite films at a rate of 3000 rpm for 30 s. For the stability test devices, we employed poly[bis(4-phenyl)(2,4,6-

trimethylphenyl)amine] (PTAA) doped with 4-isopropyl-4'-methyldiphenyliodonium tetrakis (pentafluorophenyl) borate (TPFB) as the hole transporting layer. Finally, 80 nm of Ag or Au was thermally evaporated as the electrode under high vacuum (<3.0 ×10^{-4} Pa). The area of each tested solar cells was 0.12 cm^2, as defined by the overlap between the patterned bottom ITO electrode (prepatterned by the ITO substrate supplier, B.Tree Tech Consult Co., Ltd) and top metal electrode (patterned using a shadow mask during thermal evaporation of the top electrode).

Material characterization

Scanning electron microscopy (SEM, Nova Nano 230) and atomic force microscopy (AFM, Bruker dimension Fast Scan) with peak-force tapping mode using silicon tips (OTESPA, Bruker) were used to characterize the morphology of the perovskite films. X-ray diffraction measurement was carried out by an X-ray diffractometer (PANalytical) with Cu Kα radiation at a scan rate of 4º min^{-1}. Photoluminescence (PL) was measured by a Horiba Jobin Yvon FluoroLog-3 spectrofluorometer. A monochromatic laser with wavelength of 640 nm was used for the excitation of perovskite films. Time resolved photoluminescence (TRPL) was measured by using a Picoharp 300 stand-alone TCSPC module, and a picosecond laser diode head (PLD 800B, PicoQuant) with a wavelength of 640 nm and a frequency of 80 kHz was employed. Current-voltage (J-V) characterizations of the solar cells were carried out with Keithley 2401 source meter, under simulated one sun illumination (AM 1.5G, 100 mW cm^{-2}) (Oriel Sol3A with class AAA solar simulator, Newport) with a mask with area of 0.1 cm^2. The intensity calibration of the light was done by NREL-certified Si photodiode with a KG-5 filter. The measurement of solar cells was carried out in an ambient atmosphere without pre-conditioning such as voltage bias and light soaking and a scan rate of 0.1 V s^{-1} (-0.1 V to 1.2 V as forward scan and 1.2 V to -0.1 V as reverse scan) was used for J-V characterizations. For each condition, at least 10 devices were fabricated and measured for statistical analysis. The steady-state power output of the solar cells was calculated from the photocurrent measured under constant bias voltage operation that corresponds to a maximum power output. The incident photon-to-electron conversion efficiency (IPCE) measurement was carried out by using specially designed system (Enli tech) under AC mode (chopping frequency: 133 Hz) without bias light.

Supplementary Note 1 | Computational method

All first-principles calculations on bulk systems were performed using density functional theory (DFT) in the plane-wave/pseudopotential approach implemented in the VASP package (*1*,*2*). Exchange-correlation is described the revised Perdew-Burke-Ernzerhof generalized gradient approximation (PBEsol) (*3*,*4*) including dispersion corrections to the total energies *via* Grimme's DFT-D3 scheme (*5*,*6*). Projector-augmented-wave (PAW) pseudopotentials were used for valence-core interactions (*7*). For all bulk calculations 2x2x2 supercells were used. Plane-wave type basis sets with cut-off kinetic energies 300 eV were used. For geometry optimizations, both ionic positions and cell dimensions are allowed to relax using a conjugate-gradient algorithm until the residual forces became less than 0.02 eV/Å. A 4x4x4 *k*-mesh was used for BZ sampling centered at Γ-point.

Defect-cation interaction energies were predicted using the following expression: $E_{int} = E_{d,c} - [E_d + \mu_c]$, where $E_{d,c}$ is the total energy of the supercell containing the defect plus cation, E_d is the total energy of the system with the defect only and μ_c is the chemical potential of the cation. μ_c is predicted from total-energy/site of Na cation in the fcc phase, Ca cation in the bcc and Nd cation in the hexagonal phases.

The energy barriers of iodide migration with and without dopant cations were calculated by following the reaction path energy profile of iodine migration from one site to the neighboring iodine-vacancy defect. Cations are placed at the octahedral site of the perovskite lattice. We first relaxed the initial and final structures and then a linear interpolation was performed to construct the intermediate structures within migration event. We used 18 grid points for each energy profile calculations. The energy profiles were obtained from nudged elastic band (NEB) and constrained energy minimization methods. Energy barrier of iodine migration with and without cations are computed from the energy difference between the minimum state and saddle point.

Supplementary Note 2 | Williamson-Hall analysis

It is known that size-induced and strain-induced peak broadening vary differently as a function of Bragg angle, θ, where:

$$\beta_{size} = \frac{K\lambda}{Lcos\theta}$$

$$\beta_{strain} = 4\varepsilon \frac{sin\theta}{cos\theta}$$

where βsize and βstrain are size and strain broadening, respectively, K is a constant depending on crystallite shape, λ is the x-ray wavelength, L is the crystallite size and ε is the lattice strain. For spherical crystals with cubic symmetry, K is taken to be 0.94.

The Williamson-Hall method assumes that the total broadening, βtotal, given by the full width at half maximum (FWHM) of an individual peak, is a simple sum of the two effects, where:

$$\beta_{total} = \beta_{size} + \beta_{strain} = \frac{K\lambda}{Lcos\theta} + 4\varepsilon \frac{sin\theta}{cos\theta}$$

Multiplying throughout by cos θ gives:

$$\beta_{total} cos\theta = \frac{K\lambda}{L} + 4\varepsilon sin\theta$$

Therefore, a plot of $\beta_{total} cos\theta$ against $sin\theta$ produces a linear plot whereby the slope is proportional to the strain ε and intercept is inversely proportional to the crystallite size L. The X-ray diffraction patterns were fitted to Lorentzian distribution function. The corresponding plots in Supplementary Fig. 10 is fitted to a linear curve, and the results are summarized in Supplementary Table 3.

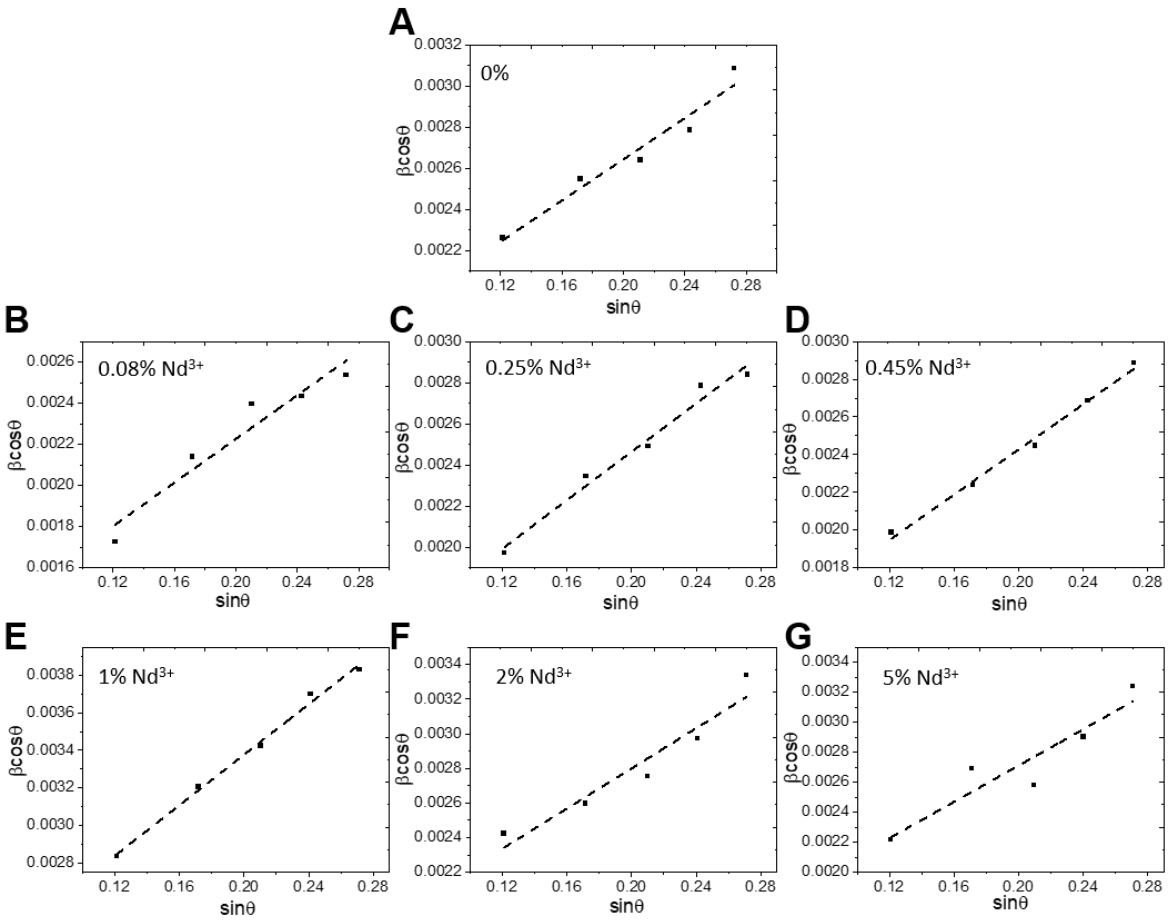

Fig. S1 | Willamson-Hall analysis of α-$FAPbI_3$ with Nd^{3+} doping concentration from 0% to 5%. The filled squares are measured data and dashed lines are fitted lines.

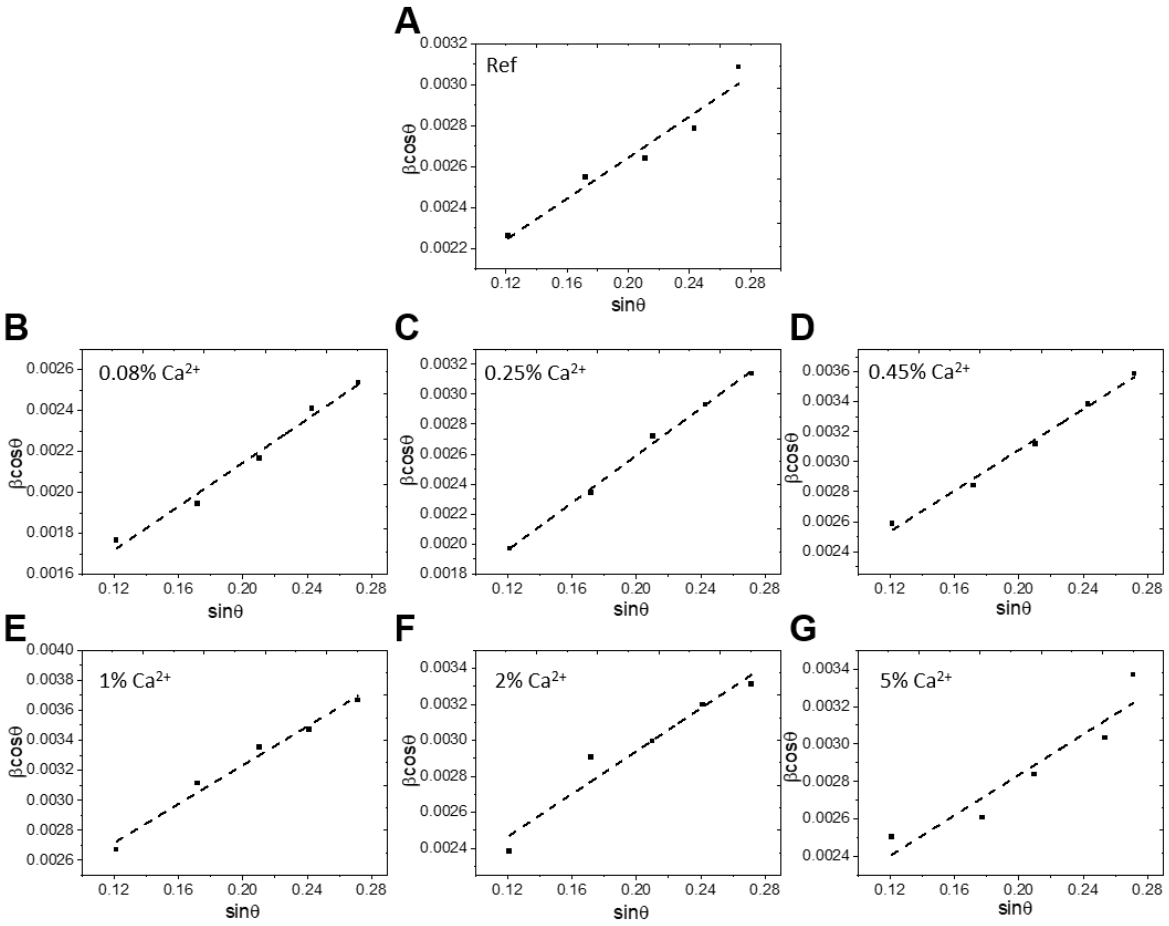

Fig. S2 | Willamson-Hall analysis of α-$FAPbI_3$ with Ca^{2+} doping concentration from 0% to 5%. The filled squares are measured data and dashed lines are fitted lines.

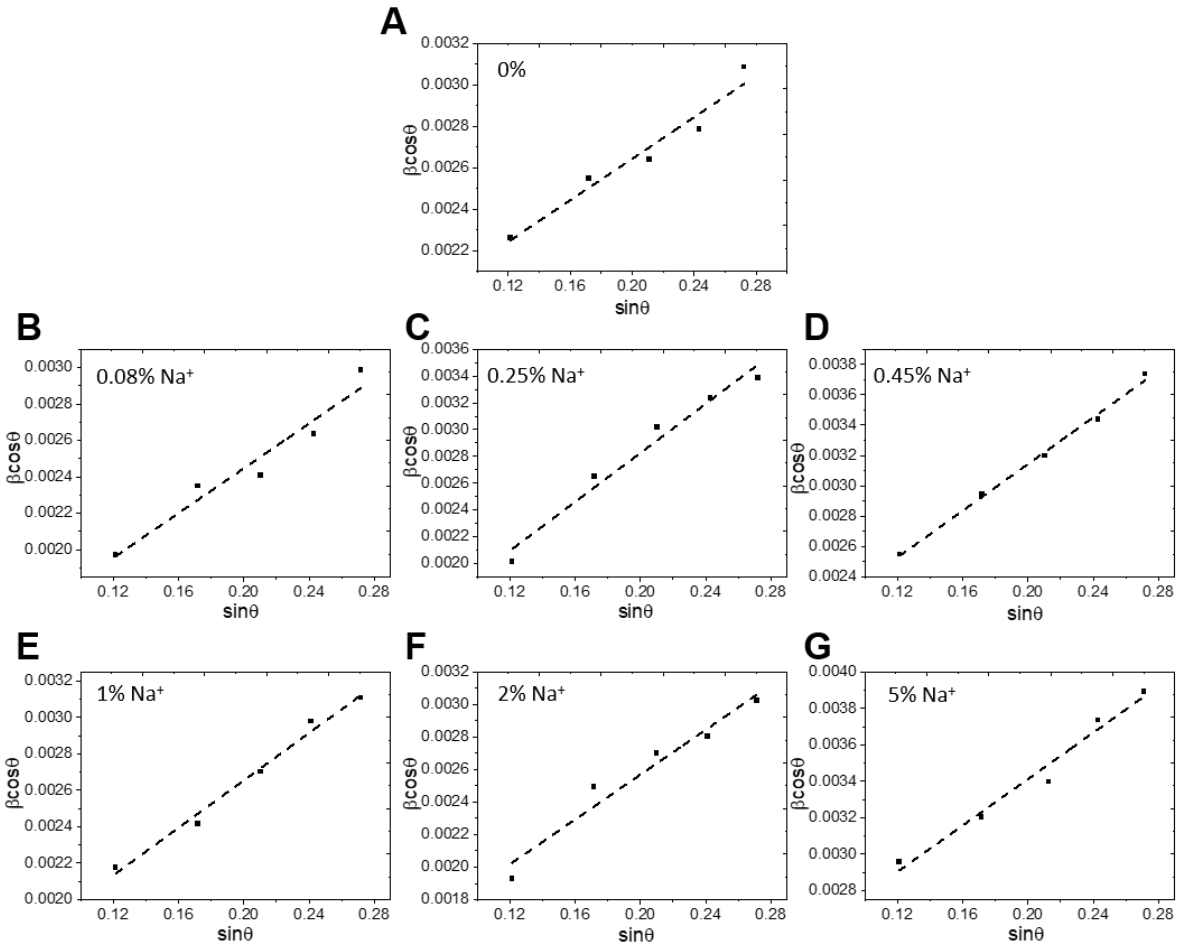

Fig. S3 | Willamson-Hall analysis of α-$FAPbI_3$ with Na^+ doping concentration from 0% to 5%. The filled squares are measured data and dashed lines are fitted lines.

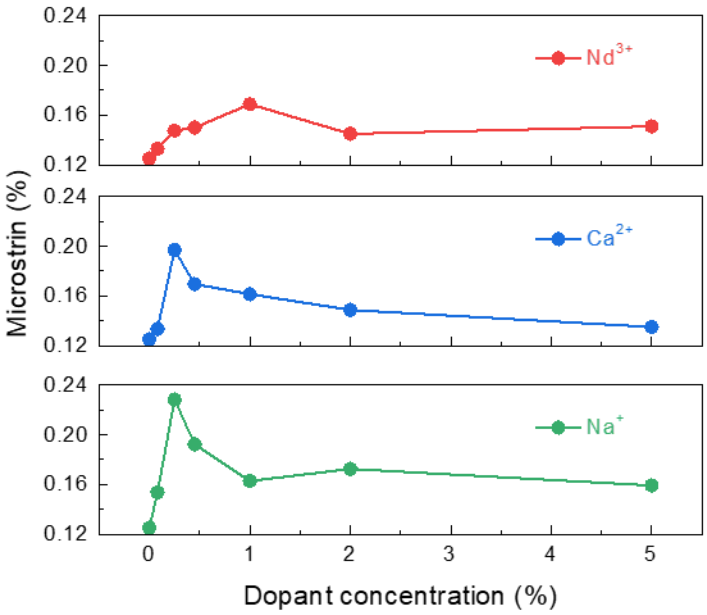

Fig. S4 | Microstrain of the α-$FAPbI_3$ with Nd^{3+}, Ca^{2+}, Na^{+} and doping concentration from 0% to 5%.

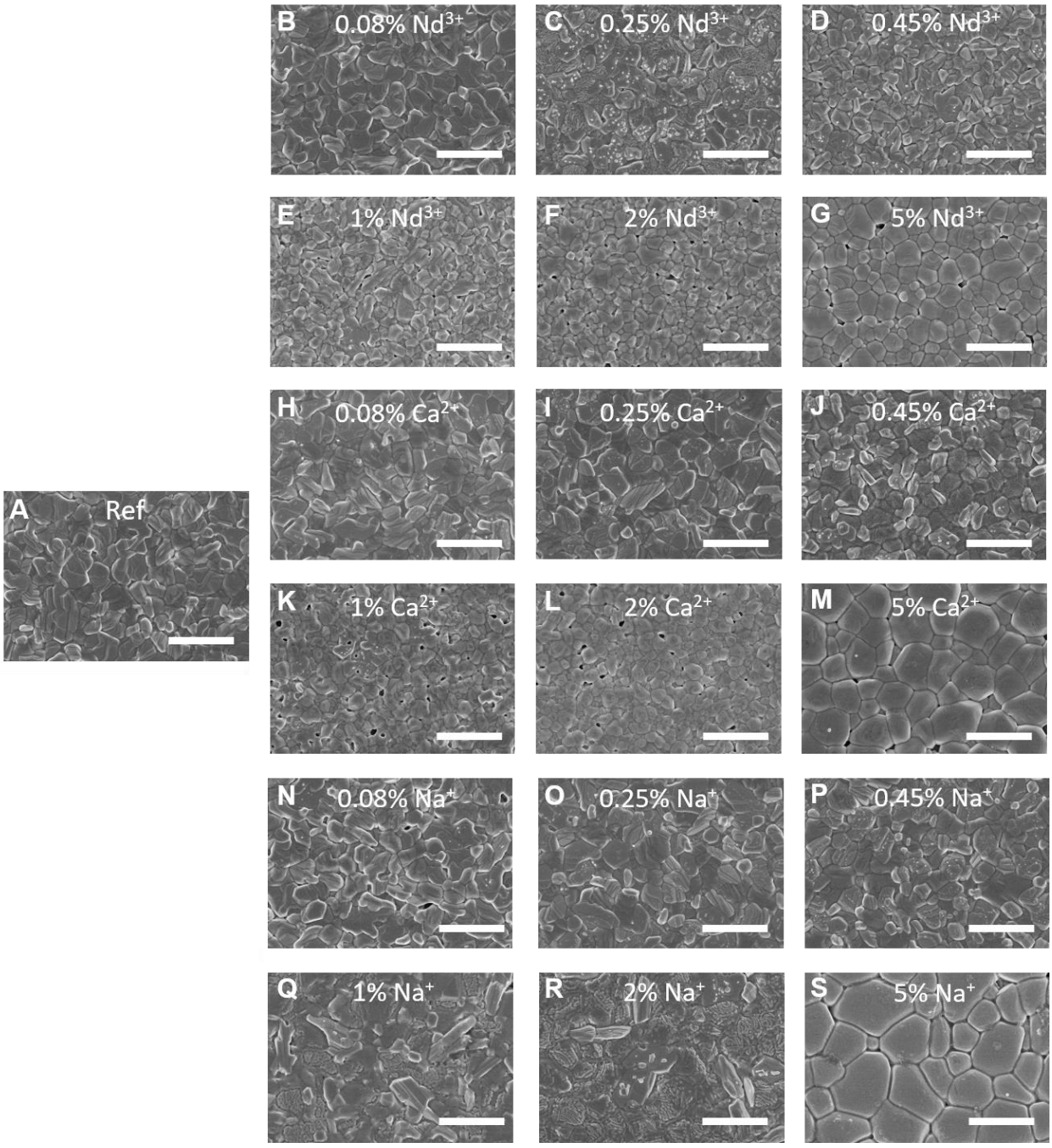

Fig. S5 | SEM images of the perovskite films without (A) and with Nd^{3+} doping concentration from 0% to 5% (B to G); B. Ca^{2+} doping concentration from 0% to 5% (H to M); and C. Na^{+} doping concentration from 0% to 5% (N to S).

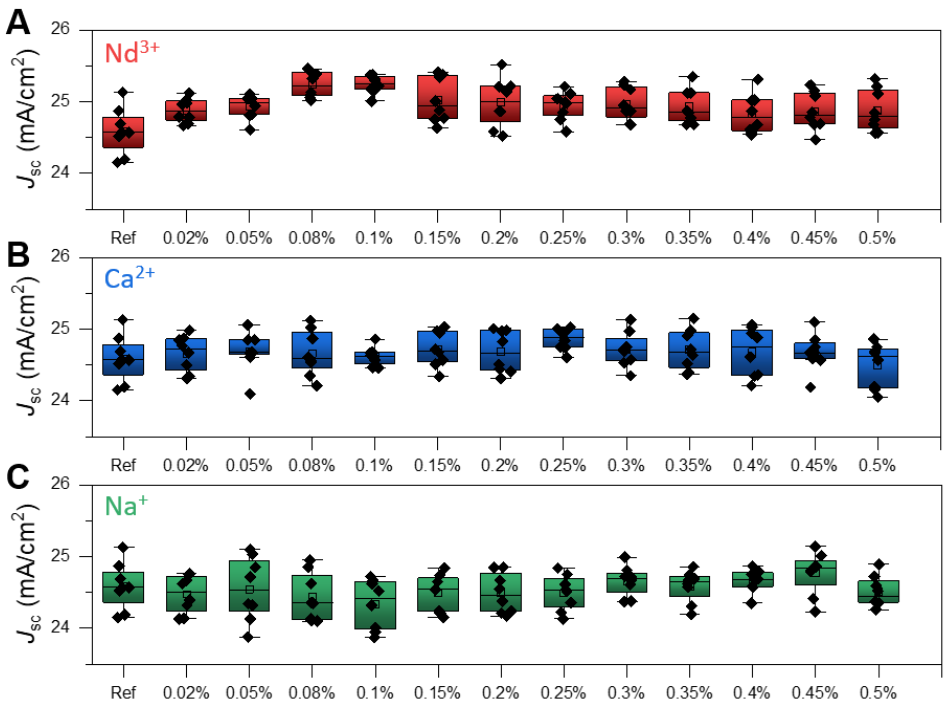

Fig. S6 | Statistical short-circuit currents (J_{sc}s) of devices with different concentrations of Nd^{3+}, Ca^{2+}, or Na^{+} incorporation.

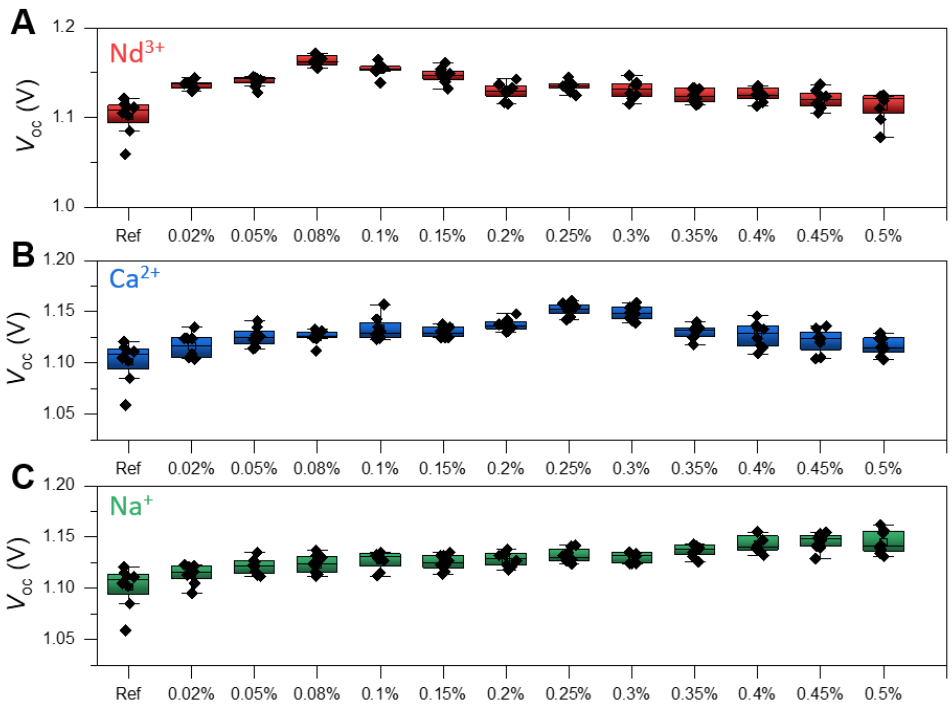

Fig. S7 | Statistical open-circuit voltages (V_{oc}s) of devices with different concentrations of Nd^{3+}, Ca^{2+}, or Na^{+} incorporation.

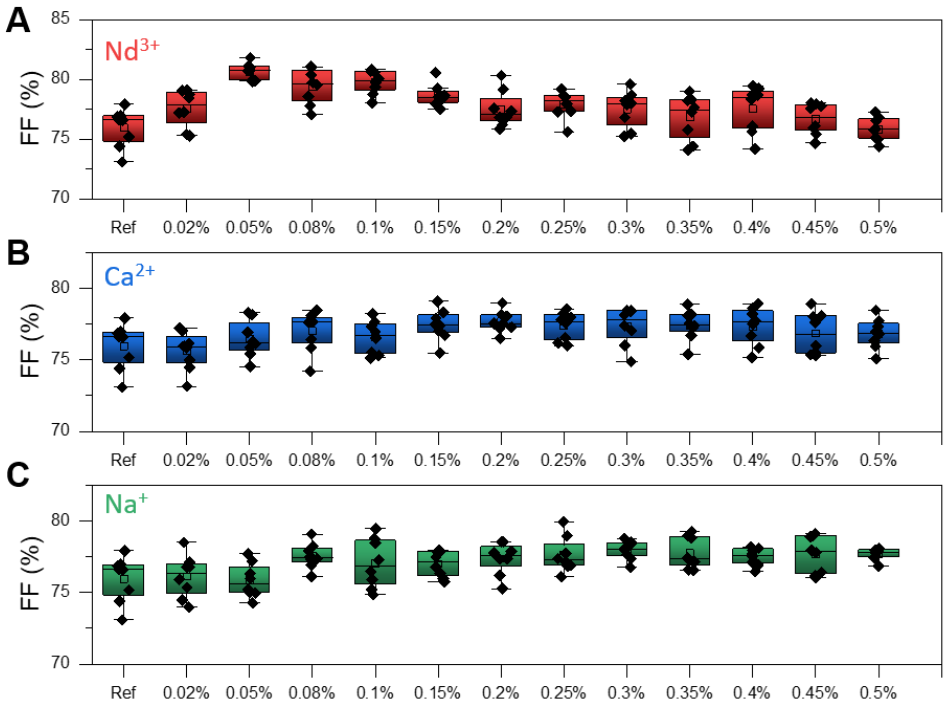

Fig. S8 | Statistical fill factors (FFs) of devices with different concentrations of Nd^{3+}, Ca^{2+}, or Na^{+} incorporation.

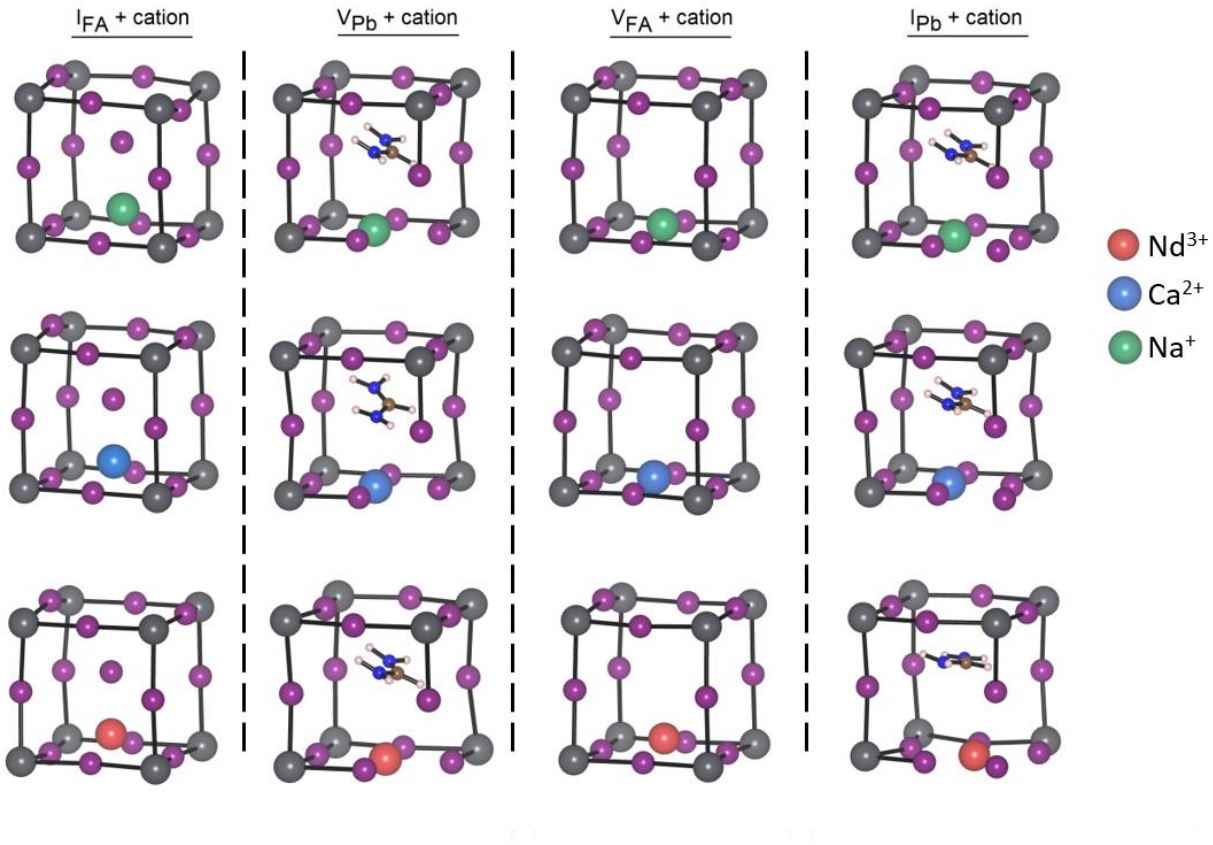

Fig. S9 | Graphical illustrations of the cations interacting with the point defects.

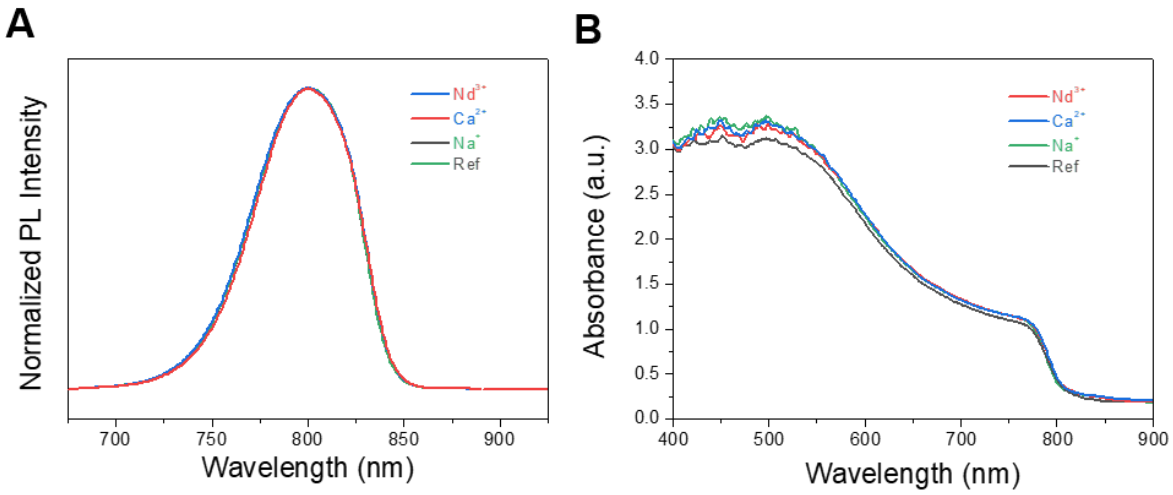

Fig. S10 | (A) Normalized PL and (B) UV-vis spectra of perovskite films without or with the optimal cation doping concentrations.

Table S1 | Fitted parameters for the data in Supplementary Fig. S1. The strain was calculated based on the function described in Supplementary Note 2.

Films	Intercept	Slope	Strain (%)
0%	0.00164	0.00501	0.125
0.08% Nd^{3+}	0.00137	0.00517	0.133
0.25% Nd^{3+}	0.00128	0.00590	0.148
0.45% Nd^{3+}	0.00102	0.00615	0.150
1% Nd^{3+}	0.00210	0.00675	0.169
2% Nd^{3+}	0.00164	0.00580	0.145
5% Nd^{3+}	0.00150	0.00604	0.151

Table S2 | Fitted parameters for the data in Supplementary Fig. S2. The strain was calculated based on the function described in Supplementary Note 2.

Films	Intercept	Slope	Strain (%)
0%	0.00164	0.00501	0.125
0.08% Ca^{2+}	0.00108	0.00534	0.134
0.25% Ca^{2+}	0.00102	0.00788	0.197
0.45% Ca^{2+}	0.00172	0.00678	0.170
1% Ca^{2+}	0.00194	0.00646	0.162
2% Ca^{2+}	0.00175	0.00595	0.149
5% Ca^{2+}	0.00176	0.00540	0.135

Table S3 | Fitted parameters for the data in Supplementary Fig. S3. The strain was calculated based on the function described in Supplementary Note 2.

Films	Intercept	Slope	Strain (%)
0%	0.00164	0.00501	0.125
0.08% Na^{3+}	0.00122	0.00615	0.154
0.25% Na^{3+}	0.00100	0.00913	0.228
0.45% Na^{3+}	0.00161	0.00769	0.192
1% Na^{3+}	0.00135	0.00651	0.163
2% Na^{3+}	0.00119	0.0069	0.173
5% Na^{3+}	0.00214	0.00637	0.159

Table S4 | Averaged photovoltaic parameters of perovskite solar cells with Nd^{3+} doping concentration from 0% to 0.5%.

Devices	V_{oc} (V)	J_{sc} (mA cm^{-2})	FF (%)	PCE (%)
Reference	1.101 ± 0.019	24.59 ± 0.30	75.95 ±1.49	20.56 ± 0.45
w/ 0.02% Nd^{3+}	1.136 ± 0.004	24.88 ± 0.16	77.55 ±1.45	21.92 ± 0.43
w/ 0.05% Nd^{3+}	1.141 ± 0.006	24.93 ± 0.16	80.64 ± 0.65	22.93 ± 0.24
w/ 0.08% Nd^{3+}	1.164 ± 0.007	25.24 ± 0.16	79.39 ± 1.38	23.31 ± 0.28
w/ 0.1% Nd^{3+}	1.154 ± 0.007	25.24 ± 0.12	79.75 ± 0.93	23.23 ± 0.34
w/ 0.15% Nd^{3+}	1.147 ± 0.008	25.02 ± 0.29	78.63 ± 0.88	22.56 ± 0.19
w/ 0.2% Nd^{3+}	1.129 ± 0.009	24.99 ± 0.32	77.50 ± 1.42	21.86 ± 0.37
w/ 0.25% Nd^{3+}	1.135 ± 0.006	24.94 ± 0.19	77.88 ± 1.06	22.04 ± 0.31
w/ 0.3% Nd^{3+}	1.131 ± 0.010	24.97 ± 0.22	77.48 ± 1.43	21.87 ± 0.28
w/ 0.35% Nd^{3+}	1.124 ± 0.007	24.93 ± 0.23	76.84 ± 1.74	21.53 ± 0.44
w/ 0.4% Nd^{3+}	1.125 ± 0.007	24.83 ± 0.26	77.53 ± 1.84	21.66 ± 0.61
w/ 0.45% Nd^{3+}	1.120 ± 0.010	24.87 ± 0.25	76.67 ± 1.21	21.35 ± 0.37
w/ 0.5% Nd^{3+}	1.113 ± 0.016	24.88 ± 0.28	75.82 ± 0.92	20.99 ± 0.42

Table S5 | Averaged photovoltaic parameters of perovskite solar cells with Ca^{2+} doping concentration from 0% to 0.5%.

Devices	V_{oc} (V)	J_{sc} (mA cm^{-2})	FF (%)	PCE (%)
Reference	1.101 ± 0.019	24.59 ± 0.30	75.95 ± 1.49	20.56 ± 0.45
w/ 0.02% Ca^{2+}	1.116 ± 0.011	24.66 ± 0.24	75.60 ± 1.27	20.81 ± 0.45
w/ 0.05% Ca^{2+}	1.125 ± 0.009	24.69 ± 0.26	76.44 ± 1.22	21.24 ± 0.53
w/ 0.08% Ca^{2+}	1.125 ± 0.006	24.66 ± 0.30	77.00 ± 1.33	21.37 ± 0.45
w/ 0.1% Ca^{2+}	1.133 ± 0.011	24.62 ± 0.12	76.57 ± 1.08	21.36 ± 0.22
w/ 0.15% Ca^{2+}	1.130 ± 0.005	24.72 ± 0.23	77.42 ± 1.02	21.63 ± 0.42
w/ 0.2% Ca^{2+}	1.137 ± 0.005	24.68 ± 0.27	77.65 ± 0.70	21.80 ± 0.39
w/ 0.25% Ca^{2+}	1.152 ± 0.006	24.87 ± 0.14	77.35 ± 0.92	22.17 ± 0.40
w/ 0.3% Ca^{2+}	1.149 ± 0.006	24.71 ± 0.23	77.34 ± 1.23	21.95 ± 0.29
w/ 0.35% Ca^{2+}	1.130 ± 0.007	24.71 ± 0.27	77.42 ± 0.99	21.62 ± 0.32
w/ 0.4% Ca^{2+}	1.127 ± 0.012	24.68 ± 0.32	77.33 ± 1.25	21.51 ± 0.49
w/ 0.45% Ca^{2+}	1.122 ± 0.011	24.67 ± 0.24	76.84 ± 1.37	21.26 ± 0.43
w/ 0.5% Ca^{2+}	1.116 ± 0.008	24.49 ± 0.29	76.82 ± 0.98	21.00 ± 0.39

Table S6 | Averaged photovoltaic parameters of perovskite solar cells with Na^+ doping concentration from 0% to 0.5%.

Devices	V_{oc} (V)	J_{sc} (mA cm^{-2})	FF (%)	PCE (%)
Reference	1.101 ± 0.019	24.59 ± 0.30	75.95 ± 1.49	20.56 ± 0.45
w/ 0.02% Na^+	1.114 ± 0.009	24.47 ± 0.24	76.11 ± 1.39	20.74 ± 0.36
w/ 0.05% Na^+	1.122 ± 0.007	24.55 ± 0.41	75.83 ± 1.11	20.87 ± 0.26
w/ 0.08% Na^+	1.124 ± 0.008	24.43 ± 0.32	77.50 ± 0.83	21.29 ± 0.37
w/ 0.1% Na^+	1.127 ± 0.008	24.34 ± 0.33	77.04 ± 1.60	21.13 ± 0.32
w/ 0.15% Na^+	1.125 ± 0.007	24.49 ± 0.24	76.99 ± 0.84	21.21 ± 0.29
w/ 0.2% Na^+	1.128 ± 0.007	24.49 ± 0.26	77.36 ± 1.06	21.38 ± 0.34
w/ 0.25% Na^+	1.132 ± 0.006	24.50 ± 0.23	77.61 ± 1.17	21.52 ± 0.34
w/ 0.3% Na^+	1.130 ± 0.005	24.66 ± 0.19	77.93 ± 0.62	21.72 ± 0.22
w/ 0.35% Na^+	1.137 ± 0.006	24.58 ± 0.21	77.74 ± 1.02	21.72 ± 0.19
w/ 0.4% Na^+	1.143 ± 0.008	24.66 ± 0.15	77.49 ± 0.57	21.84 ± 0.22
w/ 0.45% Na^+	1.146 ± 0.008	24.78 ± 0.29	77.66 ± 1.23	22.05 ± 0.18
w/ 0.5% Na^+	1.145 ± 0.011	24.51 ± 0.20	77.67 ± 0.37	21.79 ± 0.16

Table S7 | Photoluminescence lifetimes and defect density of the films without or with the optimal cation doping concentrations. Corresponding photovoltaic parameters of champion perovskite solar cells with or without dopants. The PCE values in the parenthesis are the stabilized power out (SPO) of the devices.

Devices	PL lifetime (μs)	V_{oc} (V)	J_{sc} (mA cm^{-2})	FF (%)	PCE (%)
Reference	1.68	1.121	24.87	76.58	21.35 (19.56)
w/ Nd^{3+}	7.75	1.173	25.38	79.55	23.68 (23.10)
w/ Ca^{2+}	5.47	1.162	25.01	78.56	22.83 (22.23)
w/ Na^{+}	4.78	1.148	24.93	77.96	22.31 (21.81)

References:

1. G. Kresse, J. Furthmüller, Efficiency of ab-initio Total Energy Calculations for Metals and Semiconductors Using a Plane-Wave Basis Set. *Comput. Mater. Sci.* **6**, 15−50 (1996). DOI: https://doi.org/10.1016/0927-0256(96)00008-0.

2. G. Kresse and J. Furthmüller. Efficient Iterative Schemes for ab initio Total-Energy Calculations Using a Plane-Wave Basis Set. Phys. Rev. B, **54**, 11169 (1996). DOI: https://doi.org/10.1103/PhysRevB.54.11169.

3. J. P. Perdew, K. Burke, M. Ernzerhof, Generalized Gradient Approximation Made Simple. *Phys. Rev. Lett.* **77**, 3865−3868 (1996).

4. J. P. Perdew, A. Ruzsinszky, G. I. Csonka, O. A. Vydrov, G. E. Scuseria, L. A. Constantin, X. Zhou, K. Burke, Restoring the density-gradient expansion for exchange in solids and surfaces. *Phys. Rev. Lett.* **100**, 136406 (2008). doi:10.1103/PhysRevLett.100.136406.

5. S. Grimme, Semiempirical GGA-Type Density Functional Constructed with a Long-Range Dispersion Correction, *J. Comp. Chem.* **27**, 1787–1799 (2006). doi:10.1002/jcc.20495.

6. S. Grimme, J. Antony, S. Ehrlich, S. Krieg, A Consistent and Accurate ab initio Parametrization of Density Functional Dispersion Correction (DFT-D) for the 94 Elements H-Pu, *J. Chem. Phys.* **132**, 154104 (2010). DOI: 10.1063/1.3382344.

7. P. E. Blöchl, Projector Augmented-Wave Method, *Phys. Rev. B* **50**, 17953 (1994). DOI: https://doi.org/10.1103/PhysRevB.50.17953.